Applied Catalysis B: Environmental 209 (2017) 405–416

Contents lists available at ScienceDirect

Applied Catalysis B: Environmental

journal homepage: www.elsevier.com/locate/apcatb

Controlling the stability of a Fe–Ni reforming catalyst: Structural organization of the active components

Stavros Alexandros Theofanidis[a], Vladimir V. Galvita[a,*], Maarten Sabbe[a], Hilde Poelman[a], Christophe Detavernier[b], Guy B. Marin[a]

[a] Laboratory for Chemical Technology, Ghent University, Technologiepark 914, B-9052 Ghent, Belgium
[b] Department of Solid State Sciences, Ghent University, Krijgslaan 281, S1, B-9000 Ghent, Belgium

ARTICLE INFO

Article history:
Received 16 January 2017
Received in revised form 1 March 2017
Accepted 4 March 2017
Available online 6 March 2017

Keywords:
Synthesis gas
Catalyst stability
In situ XRD
Fe–Ni alloy
Methane reforming

ABSTRACT

Fe–Ni catalysts present high activity in dry reforming of methane, with high carbon resistance, but suffer from deactivation via sintering and Fe segregation. Enhanced control of the stability and activity of Fe–Ni/$MgAl_2O_4$ was achieved by means of Pd addition. The evolution of the catalyst structure during H_2 Temperature Programmed Reduction (TPR) and CO_2 Temperature Programmed Oxidation (TPO) was investigated using time-resolved in situ X-ray diffraction (XRD). During reduction of Fe–Ni–Pd supported on $MgAl_2O_4$, a core shell alloy forms at the surface, where Fe–Ni is in the core and Fe–Ni–Pd in the shell. A 0.2 wt% Pd loading or Ni:Pd molar ratio as high as 75:1 showed the best performance in terms of both activity and stability of the catalyst at 1023 K and total pressure of 101.3 kPa. Experimental results and DFT calculations showed that Pd addition to bimetallic Fe–Ni reduces the tendency of Fe to segregate to the surface of the alloy particles under methane dry reforming (DRM) conditions, due to the formation of a thin Fe–Ni–Pd surface layer. The latter acts as a barrier for Fe segregation from the core. Segregation of Fe from the trimetallic shell still occurs, but to a lesser extent as the Fe concentration is lower. This Ni:Pd molar ratio is capable of controlling the carbon formation and hence ensure high catalyst activity of 24.8 mmol s^{-1} $g_{metals}{}^{-1}$ after 21 h time-on-stream.

© 2017 Elsevier B.V. All rights reserved.

1. Introduction

Global climate changes impose the need to investigate new routes for utilization of available resources such as natural gas, to produce fuels and chemicals [1]. Methane originates from petroleum reserves and landfill gas [2], and its conversion to higher value products will become increasingly important for the foreseeable future.

Synthesis of chemicals can be carried out via conversion of methane, either directly or indirectly. A direct process consists of one-step conversion of methane to e.g. halocarbons, hydrocyanic acid, acetylene, carbon black, aromatics, methanol or carbon disulfide. However, these processes suffer from low net yields of the desired products. This is due to the high C-H bond dissociation energy (436 kJ mol^{-1}) of the first C-H bond, making it virtually impossible to limit bond breaking to a single C-H bond [3]. Therefore, all commercial processes use methane indirectly as a feedstock for higher value products, by reforming it into syngas as an intermediate resource [4].

The most widely studied technologies for methane reforming to syngas are: steam reforming (SRM) [5,6], dry reforming (DRM) [7], partial oxidation (POM) [8,9] and autothermal reforming (ARM) [10]. The oxidant used, the final H_2:CO ratio, the kinetics and energetics differ in these processes [11,12]. Ross and co-workers concluded that among these processes DRM has a 20% lower operating cost [13] while producing high purity syngas, with low CO_2 content and H_2:CO ≤1[14]:

$$CH_4 + CO_2 \rightleftarrows 2CO + 2H_2 \quad \Delta H^0 = 261\ \text{kJ mol}^{-1} \tag{1}$$

Methane bi-reforming (BIM) on the other hand combines steam and dry reforming in one step, utilizing CH_4 and CO_2, the two most important greenhouse gases, along with H_2O to produce syngas [4,15,16]. BIM offers the advantage of a 2:1 H_2:CO ratio, named as *metgas* in order to distinguish it from syngas mixtures of different H_2:CO ratio, which is suitable for methanol synthesis [16,17]:

$$3CH_4 + CO_2 + 2H_2O \rightleftarrows 4CO + 8H_2 \quad \Delta H^0 = 220\ \text{kJ mol}^{-1} \tag{2}$$

* Corresponding author.
E-mail address: Vladimir.Galvita@UGent.be (V.V. Galvita).

http://dx.doi.org/10.1016/j.apcatb.2017.03.025
0926-3373/© 2017 Elsevier B.V. All rights reserved.

Table 1
Catalyst and support properties.

Abbreviation	Catalyst	Metal loading[a] (wt.%)			Fe:Ni (mol/mol)	Ni:Pd (mol/mol)	BET[b] (m^2/g_{cat})
		Ni	Fe	Pd	–	–	
MgAl	$MgAl_2O_4$	–	–	–	–	–	100.3 ± 5.0
0-Pd	9 wt.%Ni–4 wt.%Fe/$MgAl_2O_4$	8.4	4.30	–	0.54	–	78.0 ± 9.9
0.1-Pd	9wt.%Ni–4 wt.%Fe–0.1 wt.%Pd/$MgAl_2O_4$	9.30	4.10	0.10	0.46	171	67.7 ± 2.6
0.2-Pd	9wt.%Ni–4 wt.%Fe–0.2 wt.%Pd/$MgAl_2O_4$	8.80	3.80	0.20	0.45	75	71.0 ± 1.9
0.4-Pd	9wt.%Ni–4 wt.%Fe–0.4 wt.% Pd/$MgAl_2O_4$	8.90	3.80	0.37	0.45	44	70.3 ± 2.1
0.8-Pd	9wt.%Ni–4 wt.%Fe–0.8 wt.% Pd/$MgAl_2O_4$	7.85	3.30	0.78	0.50	21	61.3 ± 6.0
1.6-Pd	9wt.%Ni–4 wt.%Fe–1.6 wt.% Pd/$MgAl_2O_4$	7.38	3.20	1.58	0.51	8	69.4 ± 1.6

[a] ICP of as-prepared samples.
[b] As-prepared.

Side reactions of importance include the reverse water gas shift (RWGS):

$$H_2 + CO_2 \rightleftarrows H_2O + CO \quad \Delta H^0 = 41\ \text{kJ mol}^{-1} \tag{3}$$

There are certain disadvantages associated with DRM and BIM, such as high endothermicity and catalyst deactivation due to carbon deposition and sintering. The carbon deposition originates mainly from two reactions [18–20]:

$$2CO \rightleftarrows C + CO_2 \quad \Delta H^0 = -172\ \text{kJ mol}^{-1} \tag{4}$$

$$CH_4 \rightleftarrows C + 2H_2 \quad \Delta H^0 = 75\ \text{kJ mol}^{-1} \tag{5}$$

Noble metal catalysts like Pt, Rh, Pd and Ru outweigh these disadvantages: they show high activity for methane reforming and resistance toward carbon formation, but then again they are expensive [21–25]. Nickel-based catalysts have been investigated as an alternative but these are prone to deactivation due to carbon deposition, especially at CO_2/CH_4 ratios close to unity [26–28]. However, the alloy formation between Ni and other metals does lead to improved catalytic activity [29]. Addition of noble metals (Pd, Rh, Pt, Ru) to Ni-based catalysts has been investigated and alloy formation has been reported after the reduction treatment, enhancing the catalyst activity and stability [30–32]. In addition, such bimetallic catalysts often show improved dispersion, resistance against sintering and higher intrinsic reactivity compared to the original monometallic catalyst [33–36]. Damyanova and co-workers [37] investigated DRM over a series of PdNi catalysts. The higher activity observed for bimetallic Pd–Ni in comparison with monometallic catalysts was attributed to a synergetic effect between Pd and Ni resulting in higher metallic surface area and higher reducibility. Ferrandon and co-workers [38] studied steam and autothermal reforming of n-butane over Ni-Rh catalysts. They concluded that a low Rh loading in the Ni catalysts performed better than monometallic catalysts due to Ni-Rh alloy formation. Similarly, Steinhauer and co-workers [39] investigated DRM over bimetallic Ni-Pd catalysts on different supports. They also concluded that the activity of the bimetallic catalysts was higher than that of monometallics.

It has been reported that the addition of Fe as non-noble metal promoter to Ni catalysts [7] also has a beneficial impact, up to a certain Fe/Ni ratio, by suppressing carbon deposition. Fe oxide species increase the catalyst oxygen mobility, which helps to reduce carbon formation. Ashok and Kawi [40] studied toluene steam reforming over an Fe-Ni catalyst supported on Fe_2O_3-Al_2O_3. They concluded on the existence of a strong metal-support interaction which eliminated the sintering and thus resulted in stable catalyst performance. Koike et al. [41] studied the steam reforming of phenol over Fe–Ni/$MgAlO_x$ hydrotalcite catalysts and found higher activity and stability compared to the monometallic catalysts, since Fe enabled the adsorption of phenol. Fe might also improve the reducibility of Ni according to Djaidja et al. [42] who synthesized Fe–Ni/MgO and $(Fe–Ni–Mg)_2Al$ catalysts, for which the reducibility increased due to the presence of Fe. The activity results showed high performance and a good resistance against carbon formation.

Despite the positive findings with Fe–Ni/$MgAl_2O_4$ [7], for long time-on-stream (TOS > 4 h) the catalyst proved not stable during DRM at high temperature and the origin of this deactivation awaits clarification. To increase the catalyst stability, in the present work a noble metal (Pd) was added. Materials with constant Fe:Ni ratio and different Pd loadings, supported on $MgAl_2O_4$ (Fe–Ni–Pd/$MgAl_2O_4$), were used to investigate the effect of the Ni:Pd ratio upon catalyst activity and stability during DRM. The questions raised are addressed by performing X-ray diffraction (XRD) characterization of trimetallic Fe–Ni–Pd/$MgAl_2O_4$ catalysts, both ex situ and in situ during H_2 temperature-programmed reduction (TPR) and CO_2 temperature-programmed oxidation (TPO). The best candidate was also tested for activity during steam-dry reforming, using a close to bi-reforming CH_4:H_2O:CO_2 ratio, of a gas mixture which simulates the clean effluent of a biomass gasifier (after removal of tars and sulfur compounds).

2. Experimental methods

2.1. Catalyst preparation

2.1.1. Support preparation

$MgAl_2O_4$ was used as a support material and prepared by co-precipitation from an aqueous solution of $Mg(NO_3)_2{\cdot}6H_2O$ (99%, Sigma–Aldrich) and $Al(NO_3)_3{\cdot}9H_2O$ (98.5%, Sigma–Aldrich) (molar ratio Mg:Al = 1:2). NH_4OH (ACS reagent, 28.0–30.0% NH3 basis) was added as a precipitating agent to adjust the pH to 10, at 333 K. The precipitate was filtered, dried at 393 K for 12 h and subsequently calcined in air at 1023 K for 4 h.

2.1.2. Catalyst preparation

Six Fe–Ni–Pd catalysts were prepared by incipient wetness impregnation on the support ($MgAl_2O_4$) using an aqueous solution of corresponding nitrates $Ni(NO_3)_2{\cdot}6H_2O$ (99.99+%, Sigma–Aldrich), $Fe(NO_3)_3{\cdot}9H_2O$ (99.99+%, Sigma–Aldrich) and $Pd(NO_3)_2{\cdot}2H_2O$ nitrate (~40% Pd basis, Sigma–Aldrich) [43]. The catalysts were dried at 393 K for 12 h and subsequently calcined in air at 1023 K for 4 h. The molar ratio Fe:Ni was approximately stable at 0.5, while varying the loading of Pd from 0, 0.1, 0.2, 0.4, 0.8 to 1.6 wt%. Samples are labeled using their Pd content x as x-Pd as shown in Table 1. In addition, monometallic Ni (10 wt%) and Pd (0.1 wt%. 0.2 wt% and 0.5 wt%) samples were synthesized on the same support, named as "Ni" and "mono-zPd" (z equal to 0.1, 0.2 and 0.5 wt%), for comparison purposes.

2.1.3. Effect of catalyst preparation method

In view of easier characterization, Fe–Ni–Pd catalysts on the same $MgAl_2O_4$ support, with Fe:Ni molar ratio of 0.5 and higher Pd loadings (3 wt%) were prepared. Two different methods were examined, incipient wetness co-impregnation and

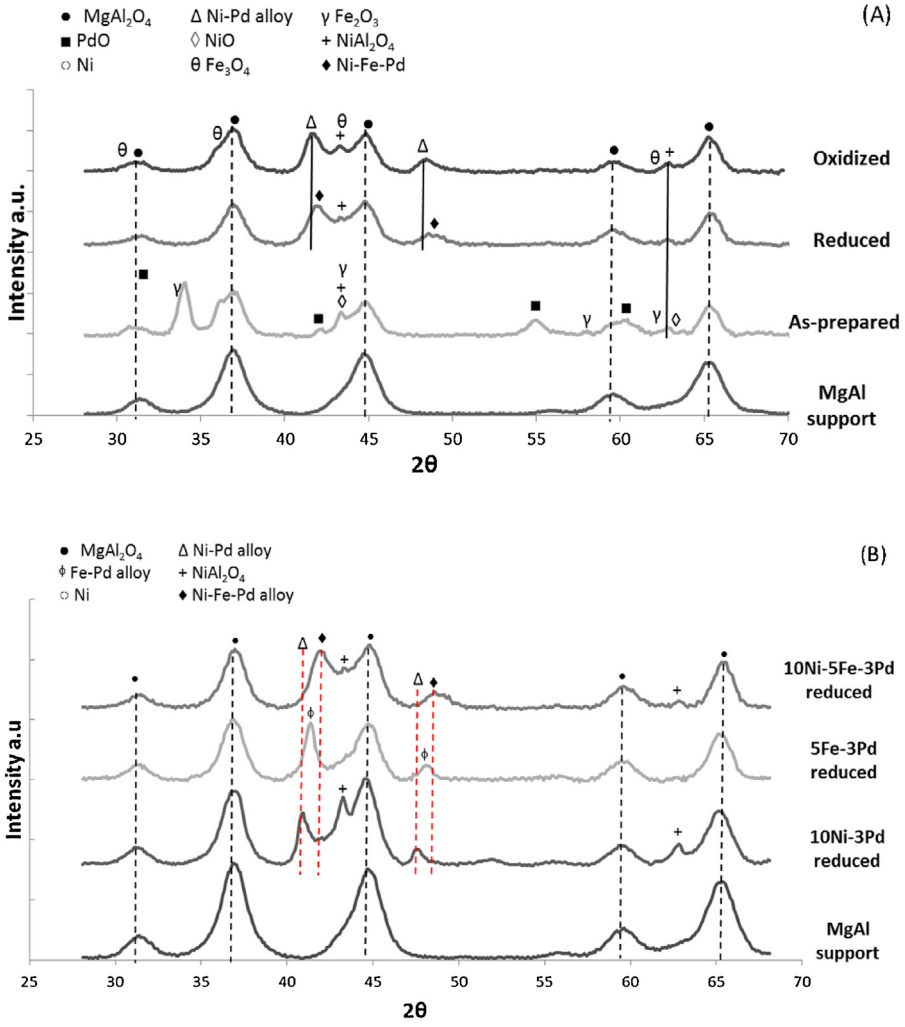

Fig. 1. Full XRD scans of (A) Fe–Ni–3Pd supported on $MgAl_2O_4$, as-prepared, reduced and oxidized (1 NmL/s of 10%H_2/He or CO_2 at a total pressure of 101.3 kPa and 1123 K). (B) Fe–Ni–3Pd reduced state along with possible bimetallic combinations (Fe–3Pd, Ni–3Pd) supported on MgAl (1 NmL/s of 10%H_2/He, at a total pressure of 101.3 kPa and 1123 K).

sequential impregnation, in order to compare the alloy that is formed after reduction treatment. During the co-impregnation, all the aforementioned precursors were mixed together (named as "Fe–Ni–3Pd"), while in case of the sequential impregnation Ni and Fe precursors were mixed first. The samples were dried at 393 K for 12 h and subsequently calcined in air at 1023 K for 4 h. Then Pd was added by incipient wetness impregnation on bimetallic Fe–Ni (named as "Fe–Ni + 3Pd"). The sample was again dried at 393 K for 12 h and subsequently calcined in air at 1023 K for 4 h. For comparison purposes, bimetallic samples, 10 wt%Ni–3 wt%Pd and 5 wt%Fe–3 wt%Pd (named as "Ni–3Pd" and "Fe–3Pd"), were equally prepared.

2.2. Catalyst characterization

The Brunauer–Emmett–Teller (BET) surface area of each sample was determined by N_2 adsorption at 77 K (five point BET method using Tristar Micromeritics) after outgassing the sample at 473 K for 2 h. The crystallographic phases of the materials as prepared were confirmed by ex situ XRD measurements (Siemens Diffractometer Kristalloflex D500, Cu Kα radiation). The powder patterns were collected in a 2θ range from 10° to 80° with a step of 0.02° and 30 s counting time per angle. XRD patterns of known compounds are referenced by their corresponding number in the Powder Diffraction File database. By fitting a Gaussian function to a diffraction peak, the crystallite size was determined from the peak width via the Scherrer equation [44], while the peak position gave information about the lattice spacing based on the Bragg law of diffraction [45].

The bulk chemical composition of support and as-prepared catalysts was determined by means of inductively coupled plasma atomic emission spectroscopy (ICP-AES, ICAP 6500, Thermo Scientific). The samples were mineralized by acid fusion.

High-resolution transmission electron microscopy (HRTEM) was used for structural analysis, while EDX yielded local chemical analysis. These techniques were implemented using a JEOL JEM-2200FS, Cs-corrected microscope operated at 200 kV, which was equipped with a Schottky-type field-emission gun (FEG) and EDX JEOL JED-2300D. All samples were deposited by immersion onto a lacey carbon film on a copper support grid.

2.3. In situ time resolved XRD

In situ XRD measurements were performed in a reactor inside a Bruker-AXS D8 Discover apparatus (Cu Kα radiation of 0.154 nm). The reactor had a Kapton foil window for X-ray transmission. The setup was equipped with a linear detector covering a range of 20° in 2θ with an angular resolution of 0.1°. The pattern acquisition time

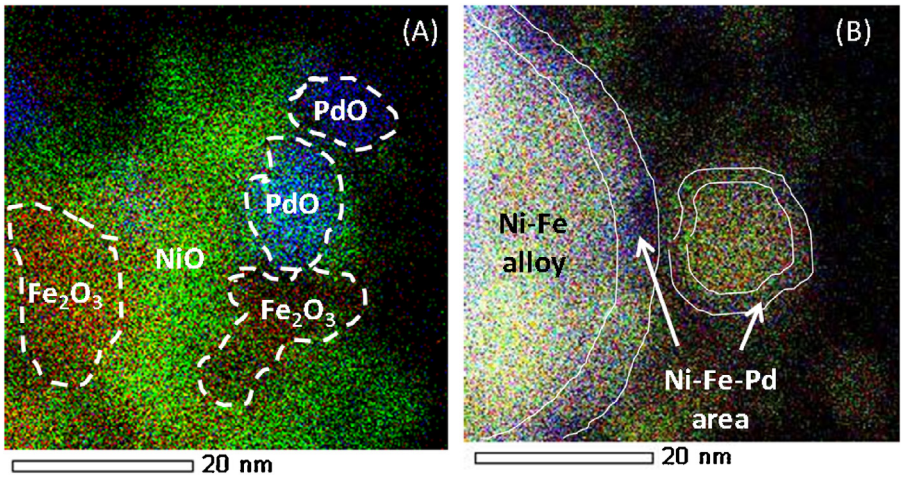

Fig. 2. EDX element mapping of 1.6-Pd. (A) as-prepared (B) reduced (1 NmL/s of 5%H_2/He mixture at a total pressure of 101.3 kPa and 1123 K). Red, green and blue colors correspond to Fe, Ni and Pd elements, respectively.

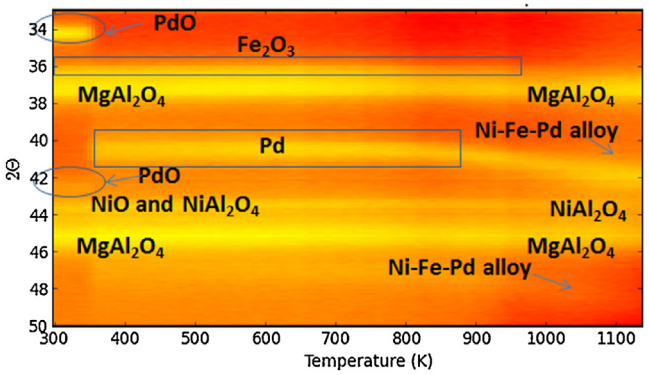

Fig. 3. 2D in situ XRD pattern during H_2-TPR for Fe–Ni–3Pd. Heating rate: 30 K/min, maximum temperature 1123 K, flow rate: 1 NmL/s, 10%H_2/He.

was 10 s. All temperatures were measured with a K-type thermocouple and corrected afterwards according to a calibration curve of the heating device, which is based on the eutectic systems Au–Si, Al–Si and Ag–Si. For each sample, approximately 10 mg of catalyst were evenly spread on a single crystal Si wafer. Interaction of the catalyst material with the Si wafer was never observed. Prior to each experiment the reactor chamber was evacuated to a base pressure of 4 Pa by a rotation pump. Gases were supplied to the reactor chamber with calibrated mass-flow controllers. He (10 NmL/s) was flowing for 10 min before the flow was switched to 5%H_2/He or CO_2 for TPR and TPO experiments (10 NmL/s, up to 1123 K, heating rate of 30 K/min, dwell time at 1123 K was 45 min), respectively.

It should be noted that the peaks in the in situ XRD patterns appeared at slightly shifted angular positions compared to both full scans and tabulated values due to temperature-induced lattice expansion and different sample heights. These shifts in peak positions which are not related to underlying physicochemical processes, were taken into account during peak assignment.

2.4. Catalytic activity

All activity measurements were performed at 1023 K and 101.3 kPa in a quartz reactor with an internal diameter of 9 mm, which was housed inside an electric furnace. The temperature of the catalyst bed was measured with K-type thermocouples touching the outside and inside of the reactor at the position of the catalyst bed. The inlet gas flow rates were always maintained by means of calibrated Bronkhorst mass flow controllers. The sample with particle size fraction of 50–125 μm was diluted with inert Al_2O_3 for improved heat conductivity (ratio catalyst:inert ~1:60) and packed between quartz wool plugs. Prior to each experiment, the as-prepared sample was reduced in a 1 NmL/s flow of 10 vol%H_2/He at 1123 K (heating rate of 20 K/min) for 30 min (named as "reduced") and then the flow was switched to 1 NmL/s of He for 20 min. A mixture of CH_4, CO_2 and He (total flow of 237 NmL/min, 37 vol% CH_4/37 vol% CO_2/26 vol% He, He as internal standard) was used as feed for DRM. The produced CO, H_2 and unconverted CH_4 and CO_2 were detected at the outlet using a calibrated OmniStar Pfeiffer mass spectrometer (MS). MS signals were recorded for all major fragments. For quantification of reactants and products, the MS was focused to different amu signals. H_2 was monitored at 2, He at 4, CH_4 at 16, H_2O at 18, C_2H_4 at 27, CO at 28 and CO_2 at 44 amu. A correction was applied to remove contributions from unavoidable interference with fragmentation peaks of other gases. To evaluate the significance of external and internal mass transfer limitations, the Carberry number [46] and Weisz-Prater criterion [47] were applied, while for heat transport limitations the Mears criteria [48] were employed.

The activity was measured as a function of time in a short term experiment (time-on-stream (TOS) = 4 h) during DRM at 1023 K and 101.3 kPa. The same conversion range ($X_{CH_4} = 50 \pm 5\%$) was achieved for all of the investigated samples by varying the amount of catalyst ($W_{metals}/F_{CH4} = 0.018 - 0.025\ kg_{metals}\ s\ mol^{-1}_{CH_4}$). With the better performing catalyst candidates, stability tests were carried out over longer TOS (24 h).

The activity was also investigated as a function of space time during isothermal bi-reforming experiments (TOS = 1 h), using a gas mixture, which simulates the clean effluent of a biomass gasifier (12.4 vol% CO, 9.8% H_2, 6.2% CO_2, 13.5% H_2O, 6.2% CH_4, 2.9% C_2H_4 and 49.0% He).

The following expressions are used to determine the activity of different catalysts. The percent conversion for a reactant is calculated as:

$$X_i = \frac{F_{in,i} - F_{out,i}}{F_{in,i}} \times 100\% \quad (6)$$

where $F_{in,i}$ and $F_{out,i}$ are the inlet and outlet molar flow rates of reactant *i*.

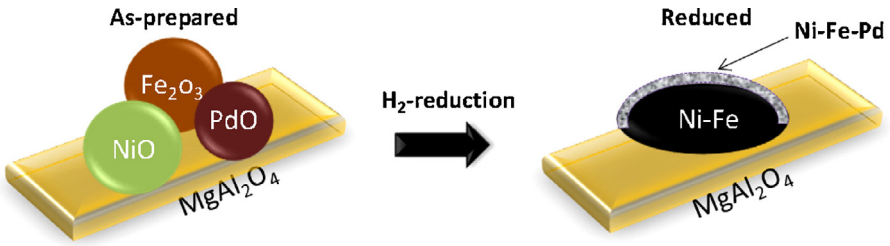

Fig. 4. Schematical representation of the alloy formation during H_2-reduction up to 1123 K.

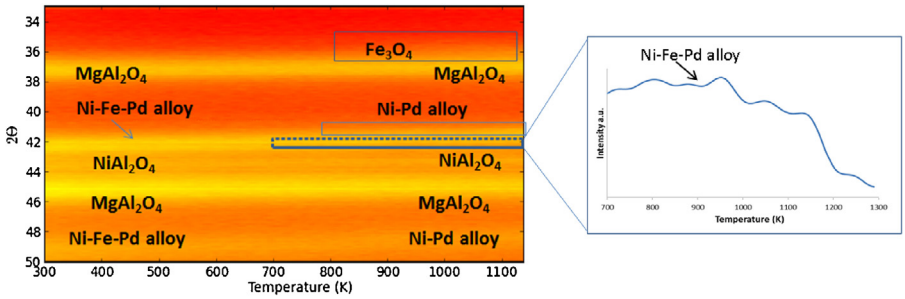

Fig. 5. 2D in situ XRD pattern during CO_2-TPO for Fe–Ni–3Pd. Heating rate: 30 K/min, maximum temperature 1123 K, flow rate: 1 NmL/s, CO_2. The highlighted rectangular area shows the integral intensity variation of trimetallic Fe–Ni–Pd alloy for diffraction angles 41.7–42.2° as a function of temperature.

The space-time yield (STY, mol s^{-1} mol^{-1}_{metals}) was calculated from the difference in the inlet and outlet molar flow rates, as measured relative to an internal standard (He).

$$\mathrm{STY}_i = \frac{\left|F_{in,i} - F_{out,i}\right|}{m_{metals}} \tag{7}$$

where F_i, mol s^{-1}, is the molar flow rate of component i and m_{metals}, the amount of Ni and Pd (g) present in the catalyst.

To determine the amount of carbon species deposited after the stability tests, TPO measurements were performed in the same experimental setup at atmospheric pressure. Once the reactor was cooled down to room temperature, the catalyst bed was subjected to a 1 NmL/s flow of 10% O_2/He. With a heating rate of 15 K/min, the temperature was raised to 1173 K. Assuming that all carbon underwent complete combustion in the presence of oxygen, the CO_2 peaks measured by MS allow calculation of the amount of carbon present on the used catalyst. TPO was carried out on all studied samples after the stability tests.

To evaluate the catalyst regeneration ability, regeneration cycles were performed after the stability tests, combining periods of oxidation by 10 vol%O_2/He, reduction by 10 vol%H_2/He and DRM at 1023 K.

2.5. Catalyst models and DFT calculations

The effect of Pd on the Fe–Ni alloy behavior in different environments was modeled using DFT calculations. Two scenarios were examined, a Fe–Ni alloy without Pd and a Fe–Ni–Pd alloy. In the studied catalysts, the molar Fe:Ni ratio is around 0.5, regardless of the presence of Pd. In the overall trimetallic alloy composition, there is at most 1 Pd per 8 Ni atoms, yet the experimentally observed Pd-rich shell will possess a higher Pd:Ni ratio.

It is generally accepted that Ni_3Fe is a stable intermetallic compound with fcc structure at temperatures below 500 K [49]. At higher temperatures, the Ni_3Fe alloy is known to be in an fcc γ-phase, though there is some discussion whether it is γ-Fe, γ-Ni, or a combination of both mentioned γ-phases [49]. The Fe:Ni molar ratio of 0.33 in Ni_3Fe is smaller than the nominal ratio of 0.50 in the present samples, still it can serve as Ni–Fe alloy approximation. Then, if one Ni is substituted by 1 Pd atom, the resulting Ni_2FePd structure has the ratio of 0.50. Since Ni–Pd and Ni–Pt are known to form an fcc solid solution for the whole range of compositions [50,51], we can assume that Ni_2FePd most likely will possess an fcc structure as well.

Therefore, the Ni_3Fe structure is taken to model the Pd-free phase, and the Ni_2FePd alloy to model the Pd-rich alloy surface phase. Both are modeled as close-packed fcc structures. In the Ni_3Fe bulk unit cell, the 3 Ni atoms occupy the face-centered positions of the bulk unit cell, while the Fe atom is located at the corner of the cell. For the Ni_2FePd bulk unit cell, one of the Ni atoms in this structure is replaced by a Pd atom.

For both fcc lattices, only the close-packed (111) surface is studied since it is typically the lowest surface energy plane and hence the most abundant surface on most particles, and the subject of interest is only to calculate the qualitative segregation behavior of iron. The (111) surface is modeled by a 4-layered slab with 4 atoms per layer, constructed from the optimized bulk fcc unit cell (see Supporting Information Secion S1.1).

The thermodynamic driving force for segregation of iron to the surface is represented by the segregation energy ΔE_{seg}, defined as the difference between the energy of the segregated slab, $E_{slab,seg}$, and the energy of the non-segregated slab, E_{slab}, expressed per number of migrating solute atoms n_M (which is 1 for the considered surface unit cell) [52]:

$$\Delta E_{seg} = \frac{E_{slab.seg} - E_{slab}}{n_M} \tag{8}$$

The segregation behavior of the alloys can be dependent on the adsorbate coverage. To this end, the minimum energy configurations for several adsorbate coverages can be calculated. In line with earlier work [52,53], the segregation energy in the presence of an adsorbate, ΔE^{ads}_{seg}, is calculated as

$$\Delta E^{ads}_{seg} = \frac{E_{slab+ads,seg} - E_{slab+ads,non-seg}}{n_{\mathrm{solutesM}}} \tag{9}$$

i.e., the difference between the energy of the segregated adsorbate-covered slab $E_{\mathrm{slab+ads,seg}}$ and the energy of the non-segregated

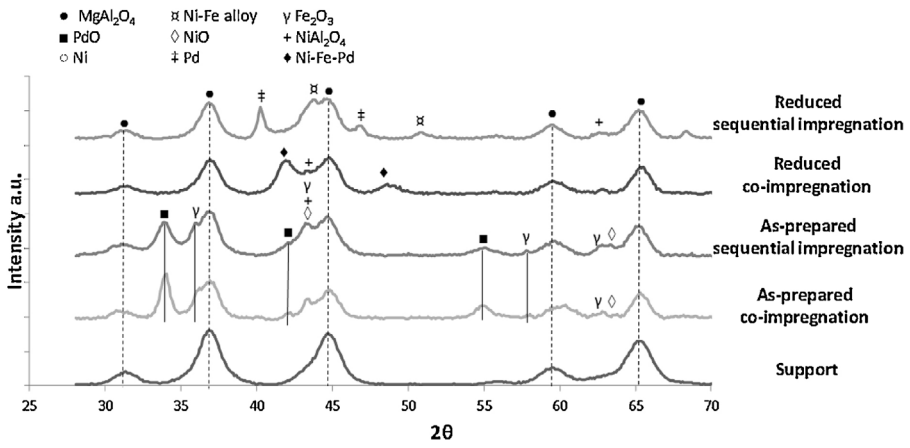

Fig. 6. Full XRD scans of Fe–Ni–3Pd and Fe–Ni + 3Pd supported on $MgAl_2O_4$, as-prepared and reduced (1 NmL/s of 10%H_2/He at a total pressure of 101.3 kPa and 1123 K).

adsorbate-coverage slab $E_{slab+ads,non-seg}$ divided by the number of migrated solute atoms, $n_{solutesM}$.

All DFT calculations have been carried out using the Perdew–Burke–Ernzerhof (PBE) GGA functional [54], with the Vienna Ab initio Simulation Package (VASP 5.3). [55–58] Details of the computational method can be found in Supporting Information Section S1.1, including details of the surface unit cells, the geometries, and the actual composition of the considered adsorbate overlayers.

3. Results and discussion

3.1. Catalyst characterization

The metal content, Brunauer–Emmett–Teller (BET) surface area, Ni:Pd and Fe:Ni ratio are reported in Table 1 for the support material and the studied catalysts. The surface area for the $MgAl_2O_4$ support has the highest value while for the catalysts it remains stable at approximately 70 m^2/g_{cat}.

The crystalline phases of as-prepared, reduced and reoxidized catalysts were determined by ex situ powder XRD. Catalysts with higher metal concentration, Fe-Ni-3Pd, were used in order to obtain more clear diffraction patterns. Fig. 1(A) displays the full scan XRD patterns of pure support, as-prepared, reduced and reoxidized Fe-Ni-3Pd catalyst. The reduced states of all the possible bimetallic combinations among Ni, Fe and Pd (Ni–3Pd and Fe–3Pd) supported on MgAl are illustrated at Fig. 1(B). $MgAl_2O_4$ (31.3°, 37°, 45°, 55.5°, 59°, 65°, Powder Diffraction File (PDF) card number: 00-021-1152) remained stable during reduction and oxidation for all samples. The "as-prepared" sample contained diffraction peaks of Fe_2O_3 (maghemite), NiO, PdO and $NiAl_2O_4$ (30.2°, 35.6°, 43.3°, 57.3° and 62.9°, PDF: 00-039-1346; 37.3°, 43.3° and 62.9°, PDF: 01-089-5881; 33.8°, 41.9°, 54.7° and 60.2°, PDF: 00-041-1107 and 37.0°, 45°, 59.7° and 65.5°, PDF: 00-010-0339), some of which are overlapping. The latter phase is in accordance with Theofanidis and co-workers [7] and Guo and co-worders [59], who found the formation of $NiAl_2O_4$ in the as-prepared sample. $NiFe_2O_4$ diffraction peaks (30.2°, 35.7°, 43.3°, 57.3°, 62.9°, PDF: 00-010-0325) overlap with those of Fe_2O_3 and therefore its presence cannot be excluded. Upon reduction, the oxides diffractions (NiO, PdO and Fe_2O_3) disappeared, while the spinel $NiAl_2O_4$ phase was not decomposed. In addition, diffractions were present at 2θ angles (42° and 48.8°) lower than those of Fe–Ni alloy (44.2° and 51.5°, PDF: 00-038-0419) [7,40,60–62]. In order to assign those shifted peaks to a crystallite structure, different bimetallic combinations among Ni, Fe and Pd, supported on the same MgAl, were examined in reduced state (Fig. 1B). The peaks observed at 42° and 48.8° in the pattern of reduced Fe–Ni–3Pd are higher than those of Fe–Pd and Ni–Pd alloy (41.2° and 47.3°, PDF: 00-002-1441 and 41.9° and 48.8°, PDF:03-065-5788), observed in the patterns of reduced bimetallic Fe-3Pd and Ni-3Pd, respectively. Therefore, the diffraction peaks at 42° and 48.8° were attributed to the formation of a trimetallic alloy phase of Ni, Fe and Pd. In the XRD pattern following the CO_2-TPO (Fig. 1A), the aforementioned trimetallic alloy phase was decomposed to Fe_3O_4 (30.1°, 35.5°, 43°, 57°, 62.5°, PDF:03-065-3107) and Ni-Pd alloy, while $NiAl_2O_4$ and MgAl support diffractions remained unchanged.

The elemental distribution of 1.6-Pd is indicated in Fig. 2, using energy-dispersive X-ray spectroscopy (EDX)-STEM mapping. In the as-prepared sample Ni (green), Fe (red) and Pd (blue) form clusters as oxides, while upon reduction the elements are redistributed, resulting in the formation of a trimetallic alloy in the outer shell. Based upon the element loadings, this implies that the core of the alloy will be close to bimetallic Ni-Fe, while the surface will be truly trimetallic Ni–Fe–Pd.

3.2. In situ XRD time resolved measurements

3.2.1. H_2-TPR

The trimetallic Fe–Ni–Pd alloy formation during the H_2-TPR process was investigated using in situ XRD measurements. A catalyst with higher concentration on metals, Fe–Ni–3Pd was used in order to obtain better signal resolution. The results are presented in a 2D in situ XRD pattern (Fig. 3). Diffraction peaks associated to Fe_2O_3 were not detected by in situ XRD due to the low concentration and their overlapping with $MgAl_2O_4$ peaks. During reduction, PdO peaks disappeared at 400 K and NiO peaks above 800 K. The $NiAl_2O_4$ spinel phase remained stable upon reduction in accordance with the ex situ XRD full scans (Fig. 1).

The characteristic peaks associated with the MgAl support did not change throughout H_2-TPR until the final temperature of 1123 K for all studied samples, implying that MgAl was not reduced in this temperature range. The Pd related diffraction shifted from 40.1° to an angle of 42.0°, above 820 K, higher than that for Ni–Pd alloy (41.9°), which was hence attributed to a trimetallic Fe–Ni–Pd alloy diffraction peak.

A graphical illustration of the Fe–Ni–Pd phase formation after catalyst reduction is depicted in Fig. 4. The alloy phase consists of a close to bimetallic core, surrounded by a thin trimetallic layer, as it was observed from EDX (Fig. 2B).

3.2.2. CO_2-TPO

The stability of the trimetallic Fe–Ni–Pd alloy active phase in oxidizing conditions was investigated during CO_2-TPO immediately after cooling down following H_2-TPR (Fig. 5). The diffraction peak

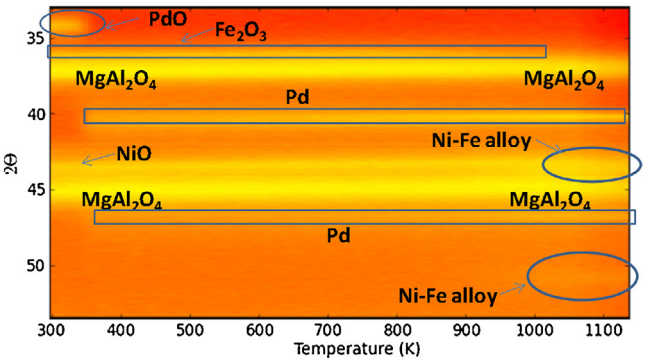

Fig. 7. 2D in situ XRD pattern during H_2-TPR for Fe–Ni + 3Pd. Heating rate: 30 K/min, maximum temperature 1123 K, flow rate: 1 NmL/s, 10%H_2/He.

assigned to the Fe–Ni–Pd alloy phase shifted to lower 2θ values above 950 K, implying the alloy decomposition to Ni–Pd alloy and Fe_3O_4, as it can be seen from the highlighted area in Fig. 5. The same result is expected in case steam would be used as an oxidizing gas. The Ni–Pd alloy remained stable up to 1123 K along with the $NiAl_2O_4$ and $MgAl_2O_4$ phases.

3.3. Effect of catalyst preparation on alloy formation

The effect of catalyst synthesis method on the formation of the trimetallic Fe–Ni–Pd alloy phase was assessed by comparing the catalyst's crystallite phases formed after co-impregnation and sequential impregnation. Fig. 6 shows the crystalline phases of as-prepared and reduced catalysts prepared by co-impregnation and sequential impregnation. The diffraction peaks of support $MgAl_2O_4$ (31.3°, 37°, 45°, 55.5°, 59°, 65°, Powder Diffraction File (PDF) card number: 00-021-1152) are the same in the as-prepared and reduced state of the samples prepared by both methods. The patterns of the as-prepared catalysts are similar for both synthesis methods, containing the diffraction peaks of Fe_2O_3 (Maghemite), NiO, $NiAl_2O_4$ and PdO phases. However, differences are apparent in the patterns of reduced catalysts. Two diffraction peaks (42° and 48.8°) are observed in the case of the co-impregnated catalyst, that were previously assigned to a trimetallic Fe–Ni–Pd alloy phase (see Fig. 1). On the other hand, two diffraction peaks at higher angles (44.2° and 51.5°) and two at lower angles (40.1° and 46.7°) are observed in the case of the catalyst prepared by sequential impregnation. These are attributed to Fe–Ni alloy (PDF: 00-038-0419) and metallic Pd (PDF: 00-046-1043), respectively, implying the crucial role of the preparation method on the trimetallic alloy phase formation.

The evolution of the catalyst structure, prepared by sequential impregnation, during H_2-TPR was examined by time-resolved in situ XRD (Fig. 7). Diffraction peaks associated to Fe_2O_3, NiO and PdO were detected in the as-prepared sample. During reduction, PdO peaks disappeared at 400 K, while the Pd related diffraction peak at 40.1° remained stable up to 1123 K, implying the absence of a trimetallic alloy phase (Fig. 3). The NiO diffraction peaks disappeared above 973 K and the Ni related peak shifted to a lower value (44.2°), which was previously assigned to a Fe–Ni alloy phase [7,40,60–62].

3.4. Activity and stability tests

3.4.1. Methane dry reforming (DRM)

The catalysts prepared by co-impregnation, where the trimetallic active phase was formed after reduction by H_2, were compared with Ni and 0-Pd samples in activity measurements during isothermal DRM at 1023 K, 101.3 kPa and CH_4:CO_2 = 1:1 in order to

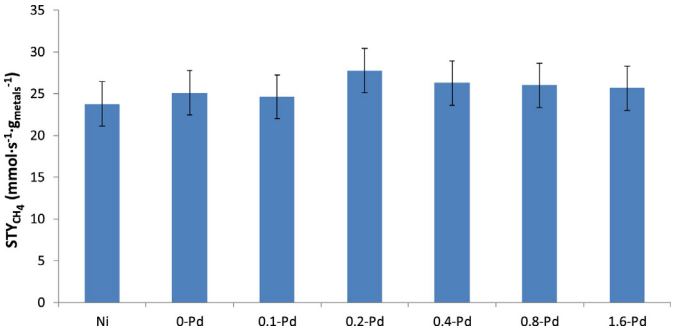

Fig. 8. Space time yield of CH_4 (STY, mmol s^{-1} g^{-1}_{metals}) of samples after 4 h time-on-stream (TOS), under DRM at 1023 K (W_{metals}/F_{CH4} = 0.018–0.025 kg_{metals} s mol_{CH4}^{-1}, total pressure of 101.3 kPa and CH_4:CO_2 = 1:1). X_{CH4} = 50 ± 5% for all studied samples. The x-Pd catalysts are trimetallic Fe–Ni–Pd samples with constant Fe:Ni ratio, containing different wt% of Pd (see Table 1). Error bars were calculated after three independent experiments representing standard deviation (68% confidence interval).

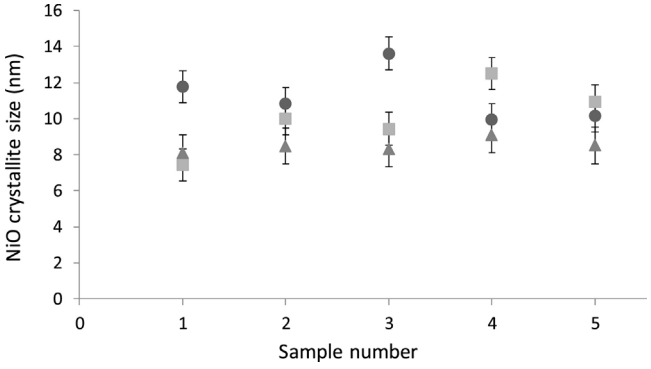

Fig. 9. Calculated NiO crystallite size (nm) from different batches of 0-Pd (●), 0.1-Pd (■) and 0.2-Pd (▲) as determined from ex situ XRD full scans.

investigate the effect of Fe-Ni-Pd alloying and Ni:Pd ratio on the catalytic properties of all studied samples. The space time yield results (STY_{CH4}) of a series of isothermal activity measurements, after TOS = 4 h, are depicted in Fig. 8.

The CH_4 space time yield for 0.2-Pd was slightly higher than the one for monometallic Ni and 0-Pd. The addition of 0.2wt%Pd (molar ratio Ni:Pd equal to 75) improved, but not significantly, the catalytic activity, while further raising the Pd concentration (or decreasing the Ni:Pd molar ratio) did not improve the activity. This is in accordance with Ferrandon and co-workers [38], who studied steam and autothermal reforming of n-butane using another noble metal, Rh, along with Ni. They found that a Rh/Ni atomic ratio close to 1/100 had the best performance, while further increase of Rh concentration did not significantly improve the catalyst activity. In literature, it is mentioned that the addition of noble metals improves the dispersion and enhances the resistance against sintering [63,64]. So, the better catalyst performance could originate from an enhanced dispersion of Ni particles due to the addition of Pd.

To assess the effect of Pd addition on NiO dispersion, five different batches of 0-Pd, 0.1-Pd and 0.2-Pd were prepared and their cystallite structure was examined using ex situ XRD. The NiO diffraction peaks were fitted with a Gaussian function and the crystallite size was estimated using the Scherrer equation [44] (Fig. 9).

The dispersion of NiO is slightly affected by Pd addition as the average crystallite size of 0.2-Pd is 8.5 ± 0.5 nm, compared to 10.0 ± 1.7 nm and 11.3 ± 1.3 nm, for 0.1-Pd and 0-Pd, respectively. This means that the activity increase observed in case of 0.2-Pd, compared to 0-Pd (Fig. 8), could indeed originate from higher dispersion of Ni.

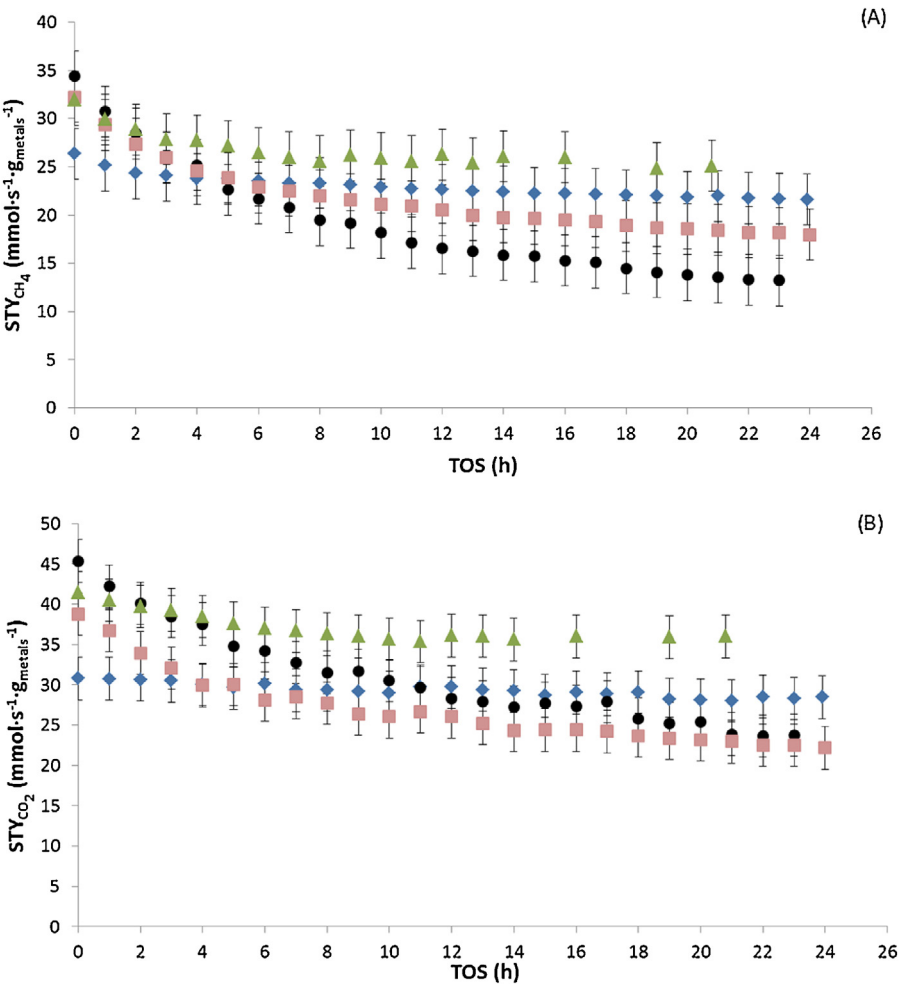

Fig. 10. Stability tests during DRM at 1023 K (total pressure of 101.3 kPa and CH_4:CO_2 = 1:1). (A): STY_{CH4} ($mmol_{CH4}$ s^{-1} g^{-1}_{metals}); (B): STY_{CO2} ($mmol_{CO2}$ s^{-1} g^{-1}_{metals}). ♦: Ni (W_{metals}/F_{CH4} = 0.022 kg_{metals} s mol^{-1}_{CH4}), X_{CH4} from 67% to 53% ●: 0-Pd (W_{metals}/F_{CH4} = 0.025 kg_{metals} s mol^{-1}_{CH4}), X_{CH4}: from 62% to 24% ■: 0.1-Pd (W_{metals}/F_{CH4} = 0.018 kg_{metals} s mol^{-1}_{CH4}), X_{CH4} from 64% to 36%; ▲: 0.2-Pd (W_{metals}/F_{CH4} = 0.024 kg_{metals} s mol^{-1}_{CH4}), X_{CH4} from 58% to 44%. Error bars were calculated after three independent experiments representing standard deviation (68% confidence interval).

In order to differentiate the contribution of the different elements to the catalyst activity, another test was performed over monometallic Pd catalysts, supported on $MgAl_2O_4$, under DRM at 1023 K (see Supporting information Figure S.2). The mono-0.2Pd catalyst reached an average CH_4 conversion of 12%, implying that Pd is active for DRM. The aforementioned result suggests that the origin of the improved activity of 0.2-Pd compared to 0-Pd (Fig. 8) includes, apart from the higher dispersion of Ni as shown in Fig. 9, the creation of extra sites upon Pd addition.

3.4.2. Stability tests

The stability of the catalysts was investigated during DRM for a TOS of 24 h. The best candidate among the studied catalysts, 0.2-Pd, was tested along with 0-Pd, 0.1-Pd and Ni for comparison purposes. CO and H_2 (see supporting information Figure S.3) as products along with unreacted CH_4 and CO_2 were observed in the reactor outlet for every studied sample. Helium was also detected as it was used as internal standard. Fig. 10 illustrates the CH_4 and CO_2 STY for all tested samples.

The pure Ni catalyst was stable during the 24 h TOS as it showed a decrease of 21% and 10% on CH_4 and CO_2 STY, respectively. However, a carbon amount of 14.7 mol_C/kg_{cat} was deposited on this pure Ni sample during 24 h TOS of DRM at 1023 K, confirmed by O_2-TPO over the used sample.

During the first 2 h TOS, 0-Pd showed the highest CH_4 and CO_2 space time yield. This is in agreement with Theofanidis and coworkers [7], who studied different Fe–Ni catalysts (Fe:Ni weight ratio from 0.7 to 1.6) supported on $MgAl_2O_4$ during DRM at 1023 K. They found that the sample with a Fe:Ni weight ratio of 0.7 had a higher CO and H_2 production and the CO:H_2 ratio was close to unity. However, after a total TOS of 24 h the 0-Pd had deactivated considerably with an activity drop of 62% and 57% for CH_4 and CO_2, respectively. Carbon deposition was examined as a possible cause of deactivation using O_2-TPO, however, no CO_2 production was detected, implying that carbon formation is not involved in the observed deactivation. This result verifies the enhanced carbon resistance of Fe-Ni catalysts that was reported elsewhere [7]. The CO:H_2 ratio increased from 1.3 after 1 h TOS to 2.5 after 24 h TOS (see Figure S.3(B)), implying a modification in the nature of active sites during the reaction.

The 0.1-Pd catalyst showed improved stability compared to 0-Pd, since the CH_4 and CO_2 space time yields decreased by 44% and 42%, respectively. However, its activity was not improved compared to 0-Pd. The best performance was observed for the 0.2-Pd catalyst, which showed the highest activity after 5 h TOS and better stability, since the CH_4 and CO_2 STY were reduced by only 23% and 20%, respectively. The produced CO:H_2 ratio was close to 1.5 (see Figure S.3), while no deposited carbon was observed over 0.2-Pd catalyst after 21 h TOS. Previously, it has been reported that

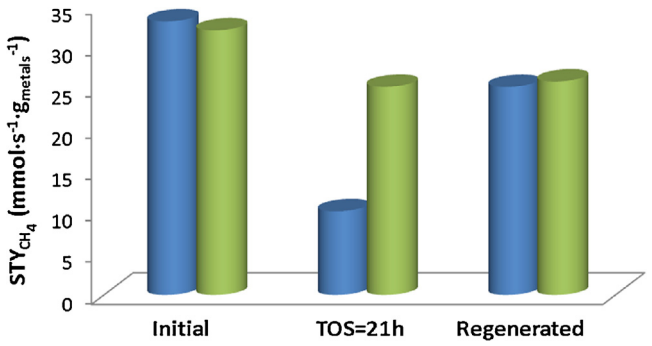

Fig. 11. Space time yield of CH_4 (STY, mmol s^{-1} g^{-1}_{metals}) of used (after TOS = 21 h shown in Figure) and regenerated 0-Pd (blue) and 0.2-Pd (green) samples under DRM at 1023 K. Catalyst regeneration took place using 10 vol%O_2/He and 10 vol%H_2/He at 1023 K and immediately after the reaction.

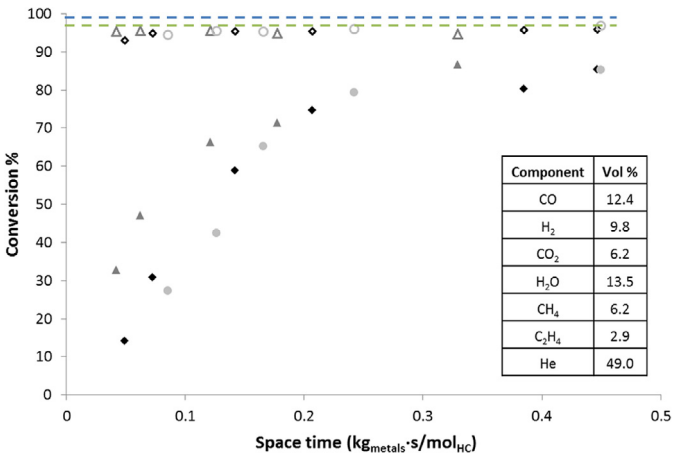

Fig. 12. Isothermal conversion of CH_4 and C_2H_4 as a function of space time during bi-reforming at 1023 K and 101.3 kPa. The solid symbols represent the CH_4 conversion while the open symbols represent the C_2H_4 conversion. ♦: Ni, ●: 0-Pd, ▲: 0.2-Pd. – – – C_2H_4 equilibrium; – – – CH_4 equilibrium. Inset table: composition of feed mixture.

bimetallic Ni-Pd catalysts (without Fe) supported on mesoporous MCM-41 do suffer from carbon deposition after DRM [37]. The absence of carbon on 0.2-Pd after long use confirms the positive effect of Fe addition on suppression of carbon formation.

To evaluate the reversibility of the deactivation, a regeneration cycle was applied after the stability tests for 0-Pd and 0.2-Pd catalysts. After regeneration, the catalyst activity was examined in situ for 2 h TOS without removing the catalyst from the reactor. Fig. 11 displays the STY of CH_4 at the beginning of the stability test presented in Fig. 10 (initial), after TOS of 21 h (used) and after regeneration of 0-Pd and 0.2-Pd catalysts.

Fig. 11 indicates that the regenerated 0.2-Pd catalyst did not recover its initial activity, remaining at a STY_{CH4} of 0.026 mol_{CH4} s^{-1} g^{-1}_{metals}, i.e. the value of STY after 21 h TOS. The latter implies an irreversible deactivation mechanism, which is attributed to sintering. On the other hand, 0-Pd recovered 76% of its initial activity after regeneration. So, in 0-Pd two parallel processes contribute to the deactivation mechanism. One is originating from sintering, and it is irreversible upon regeneration, while the other is attributed to Fe segregation from the Fe–Ni alloy, which is reversible so that the activity can be restored by Fe–Ni alloy reconstruction. Upon reuse in reaction, 0-Pd will again deactivate. However, in 0.2-Pd, the addition of Pd to Ni-Fe prevents the segregation of Fe from the Ni-Fe alloy, leaving only sintering as reason for limited activity loss in Ni-Fe-Pd.

3.4.3. *Hydrocarbons mixture bi-reforming*

The activity of the best candidate, 0.2-Pd, was further tested during bi-reforming of a hydrocarbon mixture (inset table of Fig. 12), which simulates the clean effluent of a biomass gasifier, at 1023 K and 101.3 kPa along with 0-Pd and pure Ni samples for comparison. The CH_4 and C_2H_4 conversions as a function of space time are illustrated in Fig. 12 along with the CH_4 and C_2H_4 equilibrium conversions.

At high space time value, all the samples approach the equilibrium C_2H_4 conversion, while the CH_4 conversion remains below equilibrium for all examined space time values. The differences among the catalysts are more pronounced at low space times, below 2 kg s mol^{-1}_{HC}, where the effect of C_2H_4 addition to the feed stream on CH_4 conversion can be seen. At 0.4 kg s mol^{-1}_{HC}, the CH_4 conversion of 0.2-Pd is 3 times higher than that of Ni, while at 1 kg s mol^{-1}_{HC} it is almost 2 times higher than that of 0-Pd, implying the improved performance of 0.2-Pd during bi-reforming of a CH_4 and C_2H_4 mixture. These results are in agreement with the higher activity and stability of 0.2-Pd catalyst (Figs. 8 and 10, respectively) during DRM at 1023 K and imply that a catalyst suitable for DRM can be also applied for BIM, in the presence of both CO_2 and H_2O.

4. Discussion

It is well known that Ni catalysts are prone to deactivation due to carbon deposition, especially under reforming conditions using a CH_4:CO_2 mixture with ratio near unity, which is considered thermodynamically to be a carbon-rich area [65]. The addition of Fe as a promoter to Ni catalysts has proven to be beneficial by suppressing carbon formation [7], however, after 5 h TOS the activity of the 0-Pd catalyst has dropped significantly (see Fig. 10).

Since no carbon was deposited, the origin of deactivation can be sintering, an irreversible contribution, or structural rearrangement of the surface Fe–Ni alloy, which is reversible. The ratio between reducing and oxidizing gases ($CO + H_2/CO_2 + H_2O$), R_c, is important for the iron/iron oxides system and thus for the stability of Fe containing alloys [62,66,67]. During DRM over a Fe-Ni catalyst, which proceeds following the Mars-van Krevelen mechanism, CH_4 and CO_2 are present as reactants, where CO_2 oxidizes Fe to FeO_x and CH_4 is activated on Ni [7]. The aforementioned oxidation of Fe by CO_2 during DRM at high temperature leads to its partial segregation from the alloy, even at reducing environment ($R_c > 1$). This redistribution of elements could eventually result in Fe species located on top of alloy particles. The latter follows from fast reduction of FeO_x through interaction with C, CH_x and H species at the surface. This is in agreement with Wang and co-workers, who found Fe species enriched the outer layers of alloy particles [60]. The observed deactivation can then be attributed to the high surface Fe:Ni ratio, since Fe is less active in DRM than Ni [7]. This is also in agreement with the increase of CO:H_2 ratio, observed for 0-Pd, as a function of TOS (Figure S.3(B)). A similar mechanism of deactivation can be invoked for any Fe containing alloy: it can decompose at high temperature under CO_2 [7,61,62], as it was observed in Fig. 5 for Fe–Ni–3Pd, resulting in segregation of Fe from the alloy.

A graphical illustration of the proposed deactivation for 0-Pd during DRM is depicted in Fig. 13. The Ni and Fe elements were well mixed and uniformly distributed after reduction, as it was observed elsewhere [7].

The addition of 0.2 wt% Pd (molar ratio Ni:Pd equal to 75) stabilizes the alloy core, by reconstructing its surface into a trimetallic Ni–Fe–Pd alloy. This outer layer is formed on top of the mostly bimetallic Fe–Ni core and acts as a barrier for Fe segregation from the core during reaction (see Figs. 2 and 4). As a result, only Fe located within the trimetallic alloy is accessible to CO_2 during DRM and can therefore be extracted. This is in agreement with Feli-

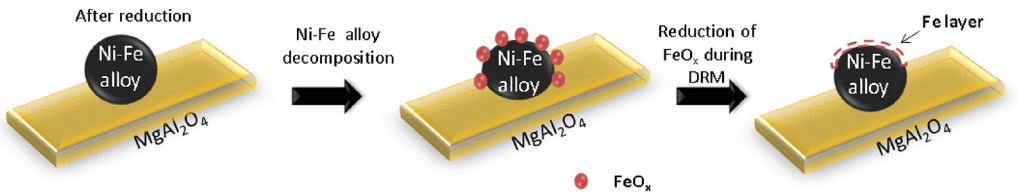

Fig. 13. Schematical representation of the proposed deactivation for 0-Pd due to Fe–Ni surface alloy reconstruction during DRM at high temperature (1023 K).

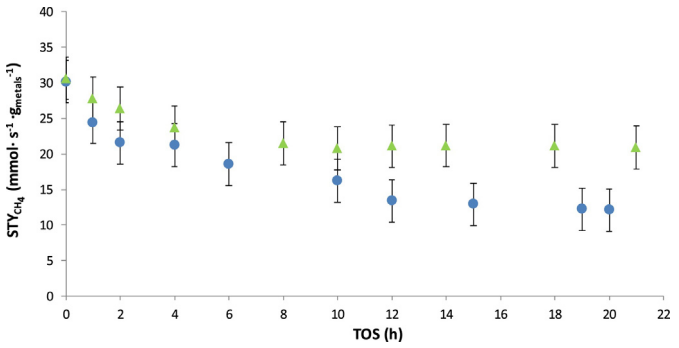

Fig. 14. Stability tests during DRM at 1023 K (total pressure of 101.3 kPa and CH_4:CO_2 = 1:1) and high initial CH_4 conversion (~80%). ●: 0-Pd (W_{metals}/F_{CH4} = 0.031 kg_{metals} s $mol^{-1}{}_{CH4}$); ▲: 0.2-Pd (W_{metals}/F_{CH4} = 0.025 kg_{metals} s $mol^{-1}{}_{CH4}$).

cissimo and co-workers [68], who investigated a Pd-Fe bimetallic model catalyst. They found that Pd forms a shell in parallel with an intermixing of Pd and Fe during the deposition of Pd on Fe particles.

In order to understand the effect of conversion, and thus of R_c, on the catalyst stability, another experiment was performed at high initial CH_4 conversion (more reducing atmosphere due to H_2 and CO presence), X_{CH4}~ 80% and R_c~16, during DRM at 1023 K over 0-Pd and 0.2-Pd (Fig. 14). The higher conversion was achieved by varying the space time.

A similar deactivation trend as in Fig. 10A was observed for 0-Pd as the activity decreased by 61%, while only 29% of activity drop was observed for 0.2-Pd. Hence, although at higher conversion a more reducing environment is present (R_c = 16), the latter does not improve the stability. This implies that the environment during DRM, at high or low conversion, does not play a role in the 0-Pd deactivation, supporting the statement that the Fe-Ni catalyst follows the Mars van Krevelen mechanism [7], where part of Fe will be oxidized by CO_2 and thus segregated from the alloy structure. This is in alignment with the result observed during an isothermal experiment using time-resolved in situ XRD, under different R_c (see Figure S.1).

To evaluate whether the thermodynamic tendency of Fe to move toward the alloy surface is reduced in the presence of Pd, the iron segregation energies were calculated using Density Functional Theory for the simplified models Ni_3Fe(111), as Fe-Ni alloy, and

Table 2
Segregation energies without (ΔE_{seg}, kJ mol^{-1}) and with adsorbates (ΔE_{seg}^{ads}) for the exchange of Fe in the subsurface layer of a (111) surface of Ni_3Fe or Ni_2FePd, with Ni or Pd from the surface layer, for various coverages, representative for DRM. All coverages refer to the species adsorbed on the fcc sites of a periodically repeated unit cell with 4 surface atoms.

ΔE_{seg} (kJ mol^{-1})	Ni_3Fe	Ni_2PdFe	
Adsorbate overlayer	Fe ↔ Ni	Fe ↔ Ni	Fe ↔ Pd
0% (vacuum)	+55	+53	+104
100% H	+49	+52	+43
100% CO	+29	+42	+3
100% O	−94	−76	−218
50% CO, 50% O	−25	−8	−92
50% CO, 25% O, 25% H	+1	+11	+38
25% of CH, CO, O, H	+2	+9	+143

Ni_2FePd (111), representing the Pd-rich shell of the alloy particle. For both model systems, an iron atom from the second layer was exchanged with an atom from the surface layer, i.e. Ni for the first, and Ni or Pd for the second alloy, representative of Fe migration to the surface (see Supporting Information Section 1.3 for details of the structures and adsorption sites). Under vacuum conditions, in the absence of adsorbates on the metal, segregation of Fe to the surface is not favorable, particularly not in exchange for a Pd atom, with segregation energies up to +100 kJ mol^{-1} (see Table 2). The presence of a monolayer of hydrogen or CO does not change this, with the only difference that exchanging a subsurface Fe for a surface Pd becomes more likely, to almost energy-neutral for CO monolayer coverage. The presence of an oxygen monolayer, which can form upon CO_2 dissociation, turns this picture upside-down: it entails a strong tendency to extract a Fe from the bulk to the surface, with segregation energies from −76 to −218 kJ mol^{-1}. However, as under DRM conditions the formation of a monolayer of oxygen is highly unlikely, more realistic coverages, containing a mixture of adsorbed CO, O, CH and H, were investigated. From the moment the fractional oxygen coverage falls to 0.25 or below, with CO, CH and H making up the remaining coverage, the segregation of Fe to the surface is almost energy-neutral, except for the exchange with surface Pd, for which the segregation energy still amounts to +38 to +143 kJ mol^{-1}.

The DFT calculations therefore indicate that (i) the segregation behavior of Fe is a very strong function of the adsorbate layer present, and (ii) the presence of Pd in a Fe–Ni alloy will reduce the tendency of Fe to segregate to the surface for coverages that

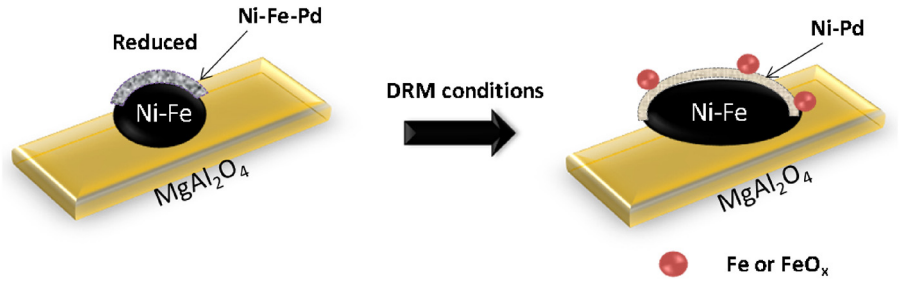

Fig. 15. Schematical representation of the proposed structure of Pd-modified samples (i.e. 0.2-Pd) during DRM at high temperature (1023 K).

are close to what can be expected during DRM conditions, which can explain the improved deactivation behavior of the Fe–Ni–Pd catalysts.

All of the above leads to the statement that the 0-Pd catalyst mainly deactivates due to extraction of Fe from the Fe–Ni alloy during DRM. The addition of 0.2 wt% of Pd to Fe–Ni forms a trimetallic layer at the surface of the particles, leading to a more bimetallic Ni–Fe core with a trimetallic Ni-Fe-Pd shell. The latter suppresses segregation of Fe from within the core to the surface. Fig. 15 illustrates in a schematical representation the structure of the Pd-modified samples under reforming conditions.

5. Conclusions

Although a Fe–Ni catalyst presents high activity in DRM, with high carbon resistance, it does suffer from deactivation via sintering and Fe segregation. Therefore, enhanced control of the stability and activity of Fe-Ni/$MgAl_2O_4$ was examined by means of Pd addition. During reduction of a co-impregnated sample, a core shell alloy forms at the surface, consisting of a Fe–Ni core and a Fe–Ni–Pd shell. The alloy is decomposed during CO_2-TPO into a Ni–Pd alloy and Fe_3O_4, above 850 K.

The effect of Ni:Pd ratio on the catalytic properties of Fe–Ni/$MgAl_2O_4$ was investigated systematically by varying the Pd concentration, during DRM at 1023 K and 101.3 kPa. The addition of Pd stabilizes the Fe–Ni alloy by means of a thin Fe–Ni–Pd surface layer. The latter acts as a barrier for Fe segregation from the core during DRM. Segregation of Fe from the trimetallic shell will still occur but to a lesser extent as the Fe concentration is lower. Moreover, DFT calculations show that the presence of Pd in a Fe–Ni alloy reduces the tendency of Fe to segregate to the surface for coverages that are relevant to DRM conditions. A Ni:Pd molar ratio equal to 75 was found to be the optimal promotion as it increased both the activity and stability of the catalyst. The origin of the improved catalytic activity derives from higher Ni dispersion along with the creation of extra active sites, due to Pd addition. The best candidate was examined under bi-reforming ($CO_2 + H_2O$) at 1023 K and 101.3 kPa of a gas mixture, which simulates the clean effluent of a biomass gasifier (absence of tars and sulfur compounds), confirming that the catalyst is not only active for DRM but also for other reforming reactions, containing steam in the feed mixture.

Acknowledgments

This work was supported by the FAST industrialization by Catalyst Research and Development (FASTCARD) project, which is a Large Scale Collaborative Project supported by European Commission in the 7th Framework Programme (GA no 604277), by the "Long Term Structural Methusalem Funding by the Flemish Government" and the Interuniversity Attraction Poles Programme, IAP7/5, Belgian State–Belgian Science Policy. The authors acknowledge support from Lukas Buelens (Laboratory for Chemical Technology, Department of Engineering and Architecture, Ghent University) for the HRTEM measurements.

Appendix A. Supplementary data

Supplementary data associated with this article can be found, in the online version, at http://dx.doi.org/10.1016/j.apcatb.2017.03.025.

References

[1] M. Maestri, D.G. Vlachos, A. Beretta, G. Groppi, E. Tronconi, AICHE J. 55 (2009) 993–1008.
[2] M.P. Kohn, M.J. Castaldi, R.J. Farrauto, Appl. Catal. B 94 (2010) 125–133.
[3] A. Caballero, P.J. Perez, Chem. Soc. Rev. 42 (2013) 8809–8820.
[4] N. Kumar, M. Shojaee, J.J. Spivey, Curr. Opin. Chem. Eng. 9 (2015) 8–15.
[5] S.D. Angeli, L. Turchetti, G. Monteleone, A.A. Lemonidou, Appl. Catal. B 181 (2016) 34–46.
[6] E.T. Kho, J. Scott, R. Amal, Chem. Eng. Sci. 140 (2016) 161–170.
[7] S.A. Theofanidis, V.V. Galvita, H. Poelman, G.B. Marin, ACS Catal. (2015) 3028–3039.
[8] M.D. Salazar-Villalpando, D.A. Berry, T.H. Gardner, Int. J. Hydrogen Energy 33 (2008) 2695–2703.
[9] A. Scarabello, D. Dalle Nogare, P. Canu, R. Lanza, Appl. Catal. B 174–175 (2015) 308–322.
[10] Y. Yan, Z. Zhang, L. Zhang, X. Wang, K. Liu, Z. Yang, Int. J. Hydrogen Energy 40 (2015) 1886–1893.
[11] A.M. Gaddalla, M.E. Sommer, Chem. Eng. Sci. 44 (1989) 2825–2829.
[12] D. Pakhare, J. Spivey, Chem. Soc. Rev. 43 (2014) 7813–7837.
[13] J.R.H. Ross, Catal. Today 100 (2005) 151–158.
[14] J. Galuszka, R.N. Pandey, S. Ahmed, Catal. Today 46 (1998) 83–89.
[15] G.A. Olah, G.K.S. Prakash, A. Goeppert, J. Am. Chem. Soc. 133 (2011) 12881–12898.
[16] G.A. Olah, A. Goeppert, M. Czaun, G.K.S. Prakash, J. Am. Chem. Soc. 135 (2013) 648–650.
[17] G.A. Olah, A. Goeppert, M. Czaun, T. Mathew, R.B. May, G.K.S. Prakash, J. Am. Chem. Soc. 137 (2015) 8720–8729.
[18] I. Luisetto, S. Tuti, E. Di Bartolomeo, Int. J. Hydrogen Energ. 37 (2012) 15992–15999.
[19] S. Damyanova, B. Pawelec, K. Arishtirova, J.L.G. Fierro, Int. J. Hydrogen Energ. 37 (2012) 15966–15975.
[20] S.A. Theofanidis, R. Batchu, V.V. Galvita, H. Poelman, G.B. Marin, Appl. Catal. B 185 (2016) 42–55.
[21] V.A. Tsipouriari, A.M. Efstathiou, X.E. Verykios, J. Catal. 161 (1996) 31–42.
[22] V.A. Sadykov, E.L. Gubanova, N.N. Sazonova, S.A. Pokrovskaya, N.A. Chumakova, N.V. Mezentseva, A.S. Bobin, R.V. Gulyaev, A.V. Ishchenko, T.A. Krieger, C. Mirodatos, Catal. Today 171 (2011) 140–149.
[23] A.M. Efstathiou, A. Kladi, V.A. Tsipouriari, X.E. Verykios, J. Catal. 158 (1996) 64–75.
[24] M.C.J. Bradford, M.A. Vannice, Catal. Rev. - Sci. Eng. 41 (1999) 1–42.
[25] J. Guo, C. Xie, K. Lee, N. Guo, J.T. Miller, M.J. Janik, C. Song, ACS Catal. 1 (2011) 574–582.
[26] D.L. Trimm, Catal. Today 37 (1997) 233–238.
[27] D.L. Trimm, Catal. Today 49 (1999) 3–10.
[28] J. Ashok, S. Kawi, Int. J. Hydrogen Energy 38 (2013) 13938–13949.
[29] L. Wang, D. Li, M. Koike, H. Watanabe, Y. Xu, Y. Nakagawa, K. Tomishige, Fuel 112 (2013) 654–661.
[30] D. Li, I. Atake, T. Shishido, Y. Oumi, T. Sano, K. Takehira, J. Catal. 250 (2007) 299–312.
[31] K. Nagaoka, A. Jentys, J.A. Lercher, J. Catal. 229 (2005) 185–196.
[32] A.S. Bobin, V.A. Sadykov, V.A. Rogov, N.V. Mezentseva, G.M. Alikina, E.M. Sadovskaya, T.S. Glazneva, N.N. Sazonova, M.Y. Smirnova, S.A. Veniaminov, C. Mirodatos, V. Galvita, G.B. Marin, Top. Catal. 56 (2013) 958–968.
[33] T. Huang, W. Huang, J. Huang, P. Ji, Fuel Process. Technol. 92 (2011) 1868–1875.
[34] Z. Hou, T. Yashima, Catal. Lett. 89 (2003) 193–197.
[35] B. Pawelec, S. Damyanova, K. Arishtirova, J.L.G. Fierro, L. Petrov, Appl. Catal., A 323 (2007) 188–201.
[36] K. Nagaoka, K. Takanabe, K.-i. Aika, Appl. Catal. A 268 (2004) 151–158.
[37] S. Damyanova, B. Pawelec, K. Arishtirova, J.L.G. Fierro, C. Sener, T. Dogu, Appl. Catal. B 92 (2009) 250–261.
[38] M. Ferrandon, A.J. Kropf, T. Krause, Appl. Catal. A 379 (2010) 121–128.
[39] B. Steinhauer, M.R. Kasireddy, J. Radnik, A. Martin, Appl. Catal. A 366 (2009) 333–341.
[40] J. Ashok, S. Kawi, ACS Catal. 4 (2014) 289–301.
[41] M. Koike, D. Li, H. Watanabe, Y. Nakagawa, K. Tomishige, Appl. Catal. A 506 (2015) 151–162.
[42] A. Djaidja, H. Messaoudi, D. Kaddeche, A. Barama, Int. J. Hydrogen Energy 40 (2015) 4989–4995.
[43] J. Haber, J.H. Block, B. Delmon, Pure Appl. Chem. (1995).
[44] Scherrer, Nachr. Ges. Wiss. Göttingen (1918).
[45] W.J. Niemantsverdiet, Spectrosc. Catal. (2007).
[46] J.J. Carberry, D. White, Ind. Eng. Chem. 61 (1969) 27–35.
[47] G.F. Fromen, K. Bischoff, Chemical Reactor Analysis and Design, J. Wiley & Sons, 1990.
[48] D.E. Mears, J. Catal. 20 (1971) 127–131.
[49] G.I. Silman, Met. Sci. Heat Treat. 54 (2012) 105–112.
[50] C.E. Dahmani, M.C. Cadeville, J.M. Sanchez, J.I. Moranlopez, Phys. Rev. Lett. 55 (1985) 1208–1211.
[51] R.H. Davies, A.T. Dinsdale, J.A. Gisby, J.A.J. Robinson, S.M. Martin, Calphad 26 (2002) 229–271.
[52] M.K. Sabbe, L. Lain, M.F. Reyniers, G.B. Marin, PCCP 15 (2013) 12197–12214.
[53] Y.G. Ma, P.B. Balbuena, Surf. Sci. 603 (2009) 349–353.
[54] J.P. Perdew, K. Burke, M. Ernzerhof, Phys. Rev. Lett. 77 (1996) 3865.
[55] G. Kresse, J. Furthmüller, Comput. Mater. Sci. 6 (1996) 15.
[56] G. Kresse, J. Furthmüller, Phys. Rev. B 54 (1996) 11169.
[57] G. Kresse, J. Hafner, Phys. Rev. B 47 (1993) 558.
[58] G. Kresse, J. Hafner, Phys. Rev. B 49 (1994) 14251.
[59] J. Guo, H. Lou, H. Zhao, D. Chai, X. Zheng, Appl. Catal. A 273 (2004) 75–82.

[60] L. Wang, D. Li, M. Koike, S. Koso, Y. Nakagawa, Y. Xu, K. Tomishige, Appl. Catal. A 392 (2011) 248–255.
[61] V.V. Galvita, H. Poelman, C. Detavernier, G.B. Marin, Appl. Catal. B 164 (2015) 184–191.
[62] J. Hu, L. Buelens, S.-A. Theofanidis, V.V. Galvita, H. Poelman, G.B. Marin, J. CO_2 Util. 16 (2016) 8–16.
[63] J.C.S. Wu, H.-C. Chou, Chem. Eng. J. 148 (2009) 539–545.
[64] Z. Hou, P. Chen, H. Fang, X. Zheng, T. Yashima, Int. J. Hydrogen Energy 31 (2006) 555–561.
[65] V. Galvita, K. Sundmacher, Chem. Eng. J. 134 (2007) 168–174.
[66] L.C. Buelens, V.V. Galvita, H. Poelman, C. Detavernier, G.B. Marin, Science 354 (2016) 449–452.
[67] V.V. Galvita, H. Poelman, V. Bliznuk, C. Detavernier, G.B. Marin, Indus. Eng. Chem. Res. 52 (2013) 8416–8426.
[68] M.P. Felicissimo, O.N. Martyanov, T. Risse, H.-J. Freund, Surf. Sci. 601 (2007) 2105–2116.